


RESEARCH

Open Access



Inflammation-sensing catalase-mimicking nanozymes alleviate acute kidney injury via reversing local oxidative stress

Hong Sang Choi^{1,2†}, Ansuja Pulickal Mathew^{3,4†}, Saji Uthaman^{3,4}, Arathy Vasukutty^{3,4}, In Jin Kim², Sang Heon Suh^{1,2}, Chang Seong Kim^{1,2}, Seong Kwon Ma^{1,2}, Sontyana Adonijah Graham^{3,4}, Soo Wan Kim^{1,2}, In-Kyu Park^{3,4*†} and Eun Hui Bae^{1,2*†} 

Abstract

Background: The reactive oxygen species (ROS) and inflammation, a critical contributor to tissue damage, is well-known to be associated with various disease. The kidney is susceptible to hypoxia and vulnerable to ROS. Thus, the vicious cycle between oxidative stress and renal hypoxia critically contributes to the progression of chronic kidney disease and finally, end-stage renal disease. Thus, delivering therapeutic agents to the ROS-rich inflammation site and releasing the therapeutic agents is a feasible solution.

Results: We developed a longer-circulating, inflammation-sensing, ROS-scavenging versatile nanoplatform by stably loading catalase-mimicking 1-dodecanethiol stabilized Mn_3O_4 (dMn_3O_4) nanoparticles inside ROS-sensitive nanomicelles (PTC), resulting in an ROS-sensitive nanozyme (PTC-M). Hydrophobic dMn_3O_4 nanoparticles were loaded inside PTC micelles to prevent premature release during circulation and act as a therapeutic agent by ROS-responsive release of loaded dMn_3O_4 once it reached the inflammation site.

Conclusions: The findings of our study demonstrated the successful attenuation of inflammation and apoptosis in the IRI mice kidneys, suggesting that PTC-M nanozyme could possess promising potential in AKI therapy. This study paves the way for high-performance ROS depletion in treating various inflammation-related diseases.

Keywords: Mn_3O_4 nanoparticles, Nanozymes, Inflammation, Ischemia–reperfusion, Kidney

*Correspondence: pik96@jnu.ac.kr; baedak76@gmail.com

†Hong Sang Choi and Ansuja Pulickal Mathew contributed equally to this manuscript as first authors

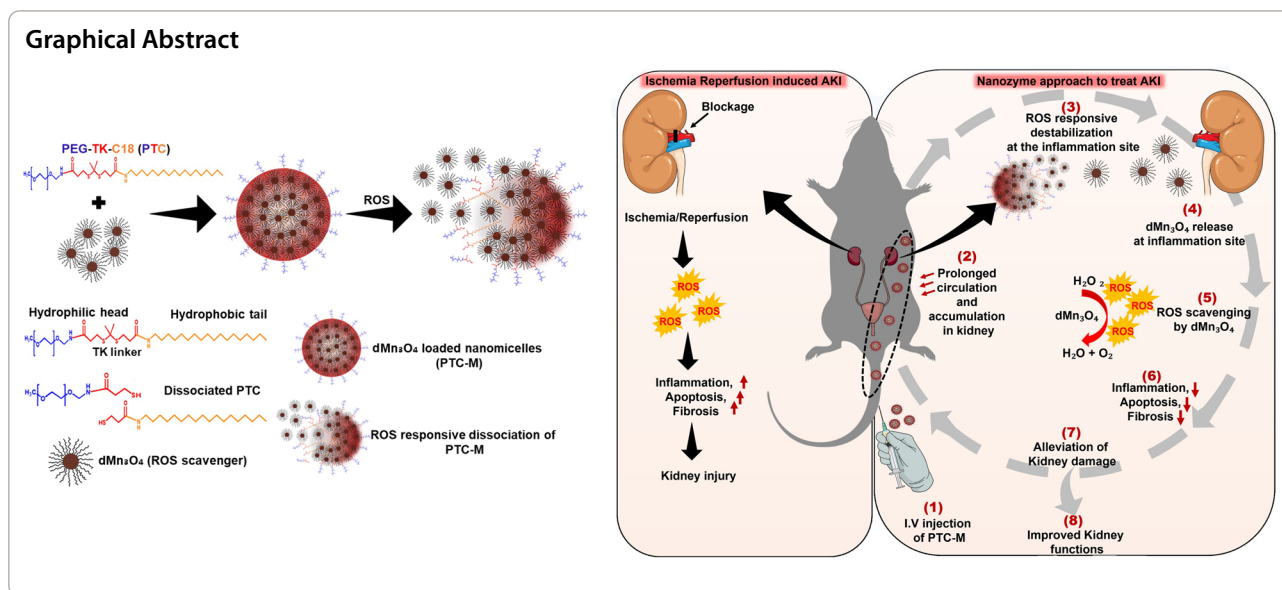
†In-Kyu Park and Eun Hui Bae contributed equally to this manuscript as correspondence authors

¹ Departments of Internal Medicine, Chonnam National University Medical School, 160, Baekseo-ro, Dong-gu, Gwangju 61469, Republic of Korea

³ Department of Biomedical Sciences, BK21 PLUS Center for Creative Biomedical Scientists, Chonnam National University Medical School, 160, Baekseo-ro, Dong-gu, Gwangju 61469, Republic of Korea

Full list of author information is available at the end of the article





Background

Acute kidney injury (AKI) is the term that covers a broad spectrum of renal function deterioration ranging from small changes in serum creatinine level to conditions requiring renal replacement therapy [1]. The KDIGO (Kidney disease: improving global outcomes) guidelines define AKI as an increase in serum creatinine of either >0.3 mg/dL within 48 h, >1.5 times from baseline within seven days, or a reduction in urine volume of <0.5 ml/kg/hour for six hours [1]. AKI is one of the rising global health problems that causes with high morbidity and mortality and economic burden [2]. The incidence of AKI defined by the KDIGO guidelines was 21.6% in adults in in-hospital settings [3]. AKI may lead to several complications, including metabolic acidosis, hyperkalemia, uremia, volume overload, and damage to other organ systems, including death. Despite advances in medicine, mortality from AKI is still high. According to a meta-analysis of studies in in-hospital settings, AKI-associated mortality was reported to be 23.9% in adults [3]. The mortality rate of dialysis-requiring AKI patients exceeds 50% [4]. AKI increases the long-term risk of subsequent AKI, progressive chronic kidney disease (CKD), and end-stage renal disease (ESRD) [5]. Eventually, AKI increases socioeconomic and healthcare burdens. Nevertheless, there is no clear treatment for AKI to date. When AKI occurs, conservative treatments such as removing the causative factors, controlling water and electrolyte imbalances, and performing renal replacement therapy, if necessary, and waiting for renal function to recover are applied.

Ischemia–reperfusion injury (IRI) is organ injury caused by the transient reduction or cessation of blood

flow, followed by reperfusion, and can be encountered in a variety of clinical situations, such as shock, myocardial infarction, ischemic stroke, major surgery, and organ transplantation. Renal IRI is one of the leading causes of AKI, which results in a rapid decline in renal function. The kidney is an organ that is particularly susceptible to ischemic insults and injured tubular epithelial cells consequently cause impaired waste product excretion, and water, electrolyte, and acid–base balance control [6]. The mechanism of renal tubular cell injury in IRI is known to involve inflammation caused by reactive oxygen species (ROS) generated during reperfusion [6–8]. Therefore, there have been attempts to apply ROS scavenging to the treatment of IRI. However, its real clinical use has been limited due to concerns for the systemic side effects, which include hypersensitivity reactions [9]. The administration of antioxidants such as edaravone has already been used to scavenge ROS in IRI. However, it was accompanied by several side effects, and hence, demands for new and effective antioxidants such as nanozymes (nanomaterials exhibiting natural enzyme-like activity) have been made [9–13]. Yao et al. found that Mn₃O₄ nanoparticles possessed multiple enzyme-mimicking activities, i.e., superoxide dismutase and catalase-mimicking activities as well as hydroxyl radical scavenging activity [11]. It was shown that Mn₃O₄ possessed a stronger ROS-scavenging ability than other nanozymes such as V₂O₅, CeO₂, Co₃O₄, MnFe₂O₄, and Fe₃O₄ and was better than that of other manganese oxide types (MnO_x (MnO₂, MnO, and Mn₂O₃)).

In this work, we developed an inflammation-sensing, ROS-scavenging versatile nanoplatfrom by stably loading catalase-mimicking dMn₃O₄ nanoparticles inside

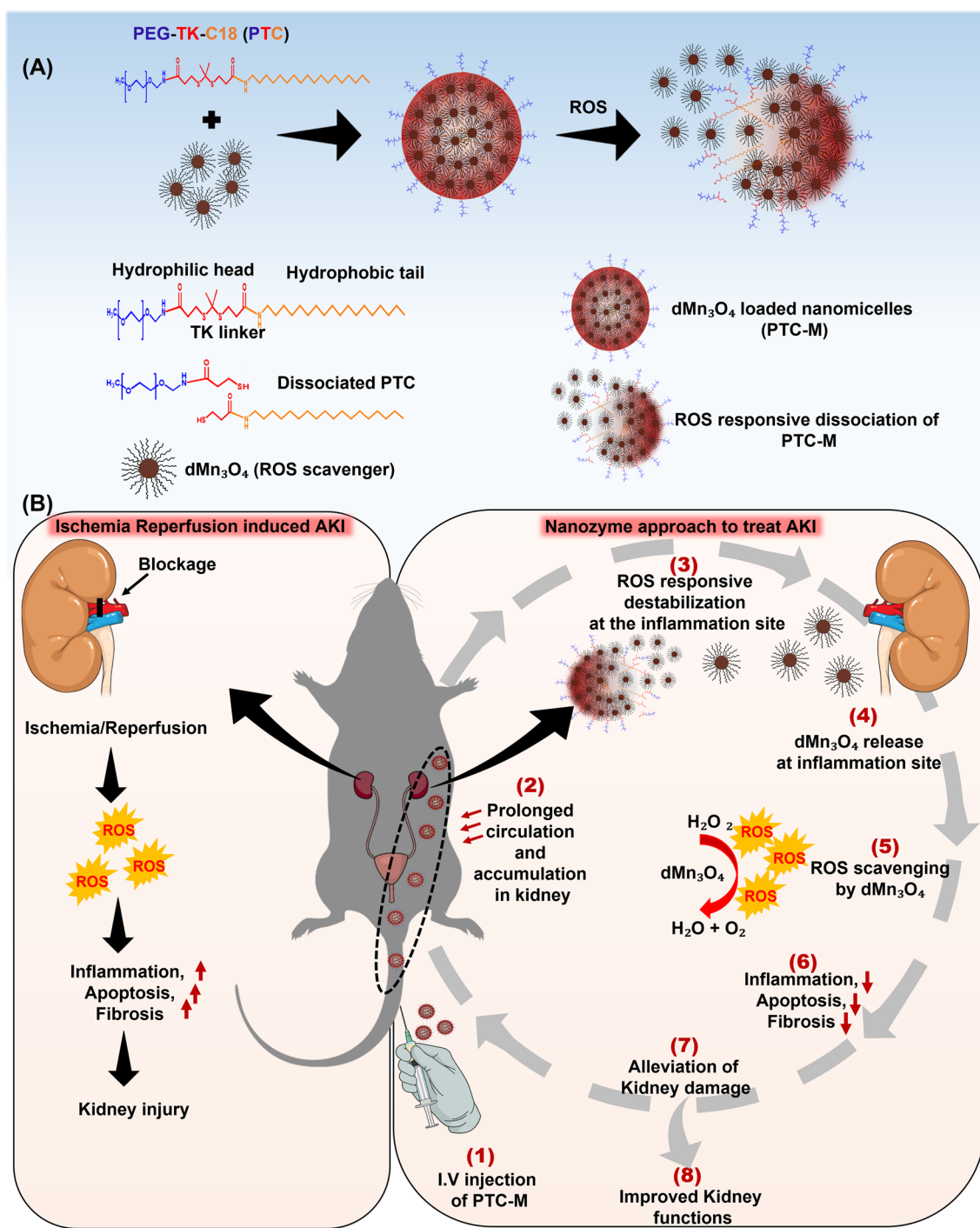


Fig. 1 Schematic illustration showing preparation and mode of action of PTC-M **A** Synthesis of PTC-M, **B** Mechanism of action of PTC-M (1) intravenous injection of PTC-M (2) the injected PTC-M circulates in blood and accumulates at the inflammation site (3) the destabilization of PTC-M due to the intrinsic ROS present at the inflammation site (4) release of the loaded dMn₃O₄ at the inflammation site (5) the released dMn₃O₄ catalyzes the ROS scavenging leading to (6) reduction in inflammation, apoptosis and fibrosis (7) alleviation of kidney damage and (8) improved kidney functions

ROS-sensitive nanomicelles (PTC), resulting in an ROS-sensitive nanozyme (PTC-M) (Fig. 1). We tried to determine if the administration of the ROS-sensitive nanozyme to the renal IRI mouse model could revert the damage caused by ROS. To the best of our knowledge, 1-dodecanethiol stabilized hydrophobic Mn_3O_4 nanoparticles (d Mn_3O_4 NPs), as well as the application of d Mn_3O_4 NPs in kidney disease, in vivo has not been reported elsewhere. We utilized the ROS-scavenging activity of the novel d Mn_3O_4 NPs to treat kidney damage. Unlike the traditional drug administration methods, the ROS-sensitive nanomicelles could deliver the d Mn_3O_4 NPs to the target organ more precisely and with fewer systemic side effects [14].

Results

Synthesis and characterization of d Mn_3O_4 nanoparticles and polymer conjugates

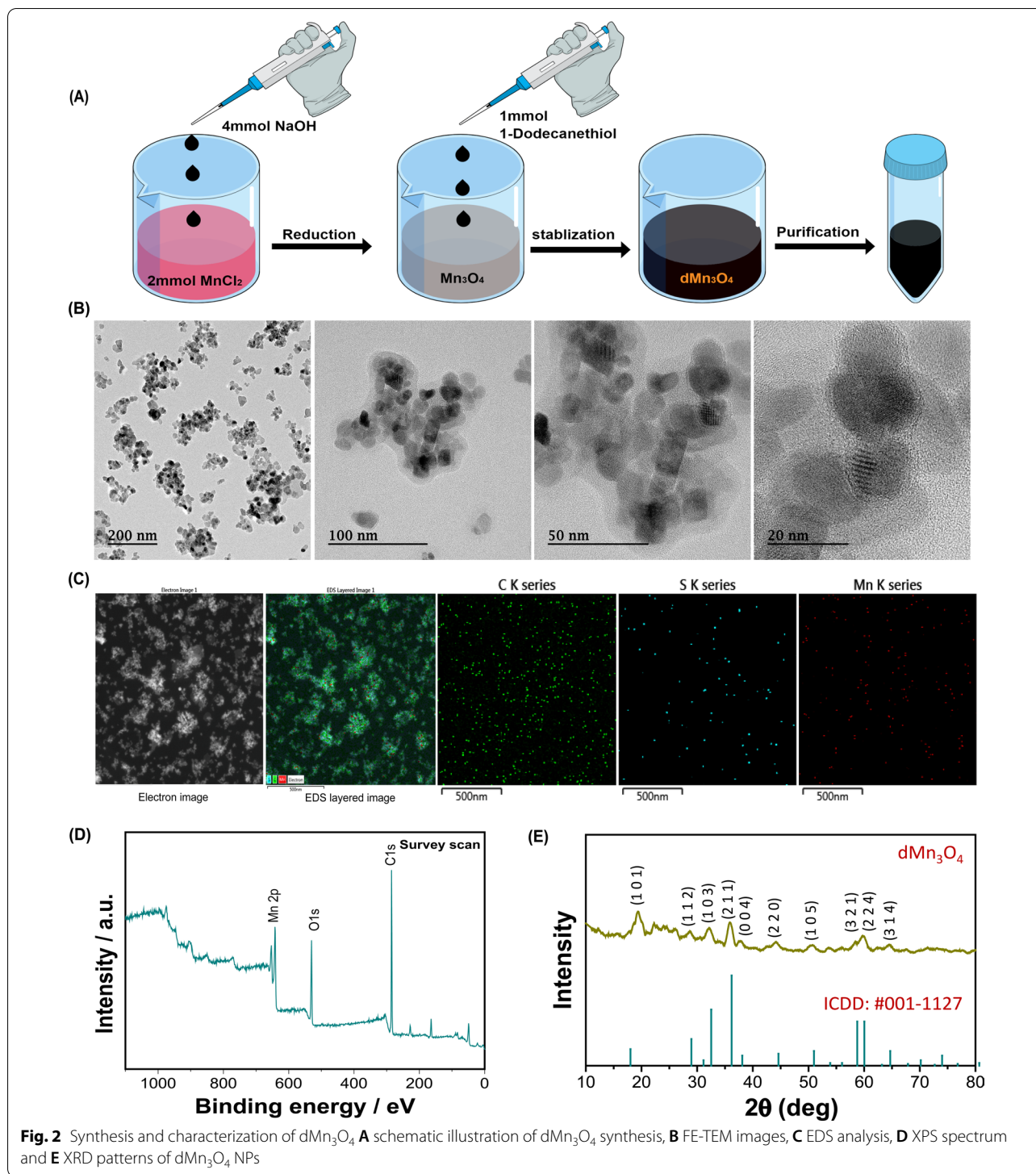
The d Mn_3O_4 NPs were synthesized using the coprecipitation method and stabilized using thiol groups of 1-dodecanethiol (Fig. 2A). Field-emission transmission electron microscopy (FE-TEM) analysis demonstrated that d Mn_3O_4 NPs had an average size less than 20 nm (18.0 ± 0.6 nm) (Fig. 2B). Additional file 1: Figure S1A and S1B show the images and schematic representation of the prepared d Mn_3O_4 . The Energy dispersive X-ray spectroscopy (EDS) data showed the presence of Mn from Mn_3O_4 and sulfur and carbon from SH-C12 (Fig. 2C and Additional file 1: Figure S1C). The X-ray photon spectroscopy (XPS) analysis results depicted the XPS spectrum of Mn $2p$, which consisted of two peaks located at 641.42 eV and 653.23 eV and these peaks were attributed to Mn $2p_{3/2}$ and Mn $2p_{1/2}$, respectively (Fig. 2D and Additional file 1: Figure S2). The energy gap between these two peaks was 11.81 eV, which was in good agreement with the reported literature for Mn_3O_4 . In the X-ray powder diffraction (XRD) pattern of the d Mn_3O_4 NPs, as shown in Fig. 2E, all the measured diffraction peaks matched well to the standard pattern of hausmannite Mn_3O_4 [ICDD: #001–1127], confirming their highly crystalline nature. The ROS-responsive PTC conjugate was prepared via stepwise chemical reactions where the thioketal (TK) linker with a terminal carboxylate group was synthesized first. The carboxylic group of the TK linker was then conjugated to the amino group of Methoxy-PEG amine (PEG-AM) using the EDC/NHS reaction to form PEG-TK. Finally, the other carboxylic group of PEG-TK was conjugated to the amino group of stearamine again via the EDC/NHS reaction [15]. The ROS nonresponsive PC conjugate was prepared by conjugating stearic acid to PEG-AM. The composition of PTC and PC was analyzed by ^1H nuclear magnetic resonance (NMR) spectroscopy (Additional file 1: Figure S3). The NMR spectra showed

characteristic peaks at δ 0.83 and 1.23 ppm corresponding to the methyl and methylene protons of C18. The peak at δ 3.6 corresponded to O–CH₂–CH₂- of PEG. The degree of substitution (DS %) of C18 in PTC and PC was calculated as 78% and 46%, respectively.

Preparation and characterization of PTC-M nanozyme

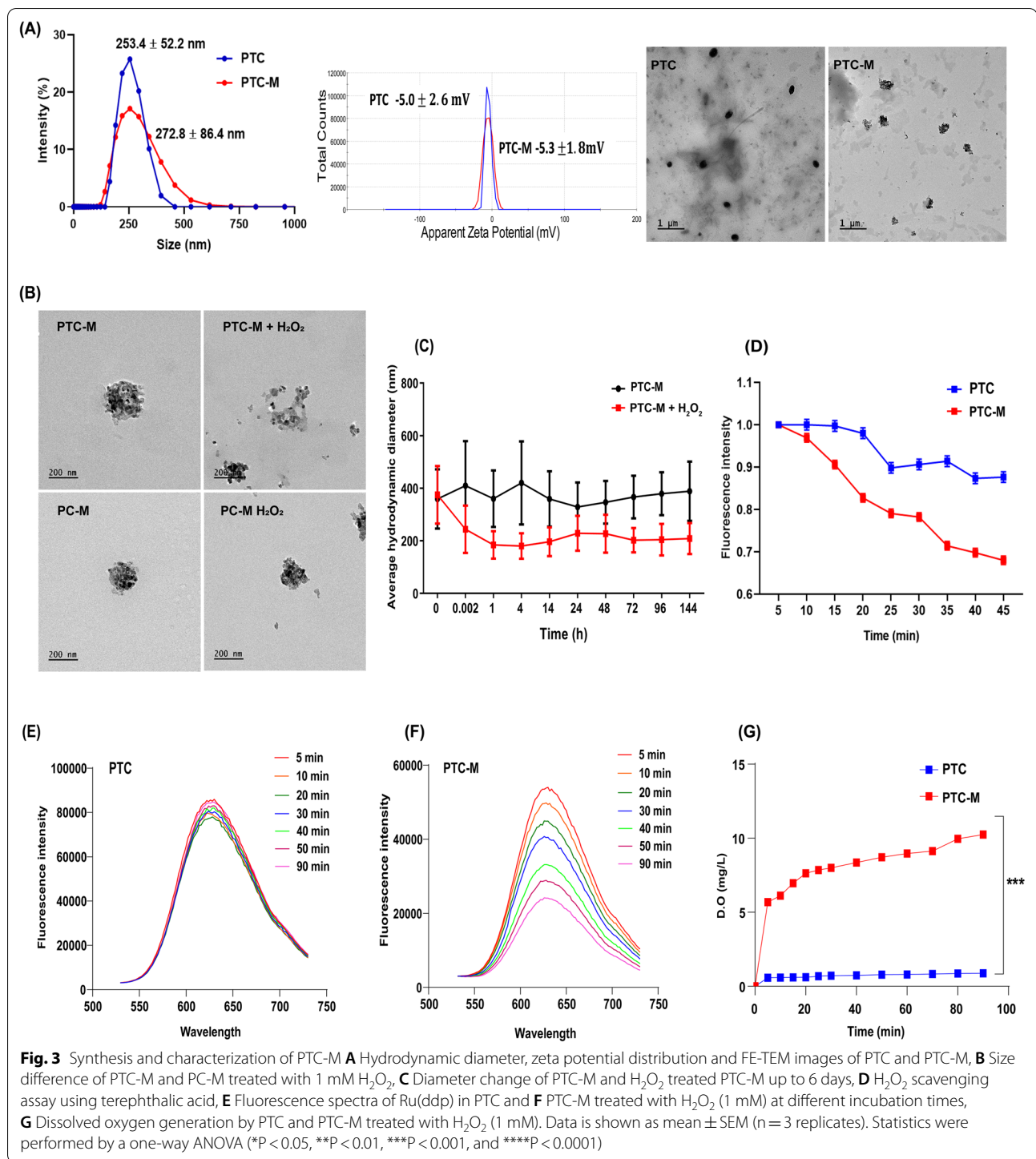
The ROS-sensitive nanomicelles (PTC) were loaded with d Mn_3O_4 , resulting in PTC-M. The d Mn_3O_4 feed ratio (20%) of PTC was utilized for the preparation of PTC-M. The hydrodynamic diameter, zeta potential, and FE-TEM images of the prepared PTC and PTC-M are shown in Fig. 3A and Additional file 1: Figure S4A. The FE-TEM images of PTC demonstrated spherical nanomicelles with uniform particle sizes. The hydrodynamic diameter of PTC-M was slightly increased after the loading of d Mn_3O_4 because of the packing of d Mn_3O_4 in the hydrophobic space while the zeta potential stayed negative in both nanomicelles due to PEG shielding. The FE-TEM images of PTC and PTC-M showed uniformly distributed particles. The loading content and encapsulation efficiency were calculated using mass spectrometric analysis and were calculated to be $10 \pm 3\%$ and $17 \pm 6\%$, respectively. The presence of d Mn_3O_4 was clearly visible in the FE-TEM images of PTC-M (Fig. 3A), which was further confirmed by EDS analysis of PTC-M, showing Mn from Mn_3O_4 , sulfur and carbon from SH-C12, and carbon, nitrogen, and oxygen from PEG (Additional file 1: Figure S5). Thermogravimetric (TGA) analysis was performed and the d Mn_3O_4 loading was calculated to be 12% (Additional file 1: Figure S6B). ROS-non-sensitive micelles loaded with d Mn_3O_4 (PC-M) were also prepared as controls by the same method.

To confirm the role of TK linkage in the ROS-responsive destabilization of PTC-M and release of d Mn_3O_4 , PTC-M was exposed to ROS conditions by adding H_2O_2 . As controls, we utilized the ROS-non-sensitive PC-M. Both the PTC-M and PC-M exhibited a spherical morphology with tightly packed d Mn_3O_4 in the nanomicelles, but after H_2O_2 treatment, the supra-assembly of the PTC-M was distorted, followed by the release of d Mn_3O_4 , which was then aggregated as shown in the FE-TEM images, whereas the PC-M showed stable structures even after exposure to H_2O_2 (Fig. 3B and Additional file 1: Figure S4B). The ROS susceptibility of PTC-M was further confirmed by comparing the changes in hydrodynamic diameter and zeta potential with the PC-M, as shown in Additional file 1: Figure S7. The hydrodynamic diameter and zeta potential of the ROS-non-sensitive PC-M showed no discernible difference after the addition of H_2O_2 . However, the ROS-sensitive PTC-M showed reduced hydrodynamic sizes, probably because of the removal



of PEG shielding via TK breakage, resulting in destabilization of the structure. After the addition of H₂O₂, the zeta potential reverted from a negative to positive charge, which could be because of the removal of PEG and exposure of stearamine. We further studied the size

variation by checking the stability over time by tracking the hydrodynamic diameters in the presence or absence of H₂O₂ (Fig. 3C). After the addition of H₂O₂, the hydrodynamic diameters significantly decreased within 10 s with no further changes with time up to six



days, whereas PTC-M alone showed stable sizes during the experiment, suggesting the good colloidal stability of the PTC-M. We also checked the stability in 10% FBS and observed that the PTC-M showed good stability upto 4 days (Additional file 1: Figure S9). The hydrodynamic diameters and zeta potential variation were also

confirmed with ROS-sensitive and non-sensitive empty nanomicelles (PTC and PC) (Additional file 1: Figure S8). All these comparative studies in the presence or absence of ROS clearly demonstrated the stability and ROS sensitivity of the prepared nanomicelles or final dMn_3O_4 PTC-M nanozyme.

We further checked the H_2O_2 elimination property of the final PTC-M nanozyme due to dMn_3O_4 NP-loading. This was tested using terephthalic acid (TA) as a fluorescent probe. TA reacted with H_2O_2 to form 2-hydroxyterephthalic acid with a fluorescent peak at 425 nm. dMn_3O_4 will convert H_2O_2 to water and oxygen and hence, the fluorescent intensity decreases, confirming catalase-like activity, as shown in Fig. 3D. The PTC-M showed a strong reduction in fluorescence intensity compared to the empty micelle PTC in the presence of H_2O_2 over time. The catalase-like activity of PTC-M was also concentration-dependent, as shown in Additional file 1: Figure S10. The oxygen production capacity of PTC-M was further confirmed using an O_2 -specific fluorescent probe Ru(ddp) in the presence of H_2O_2 . The fluorescence intensity of Ru(ddp) decreases in the presence of O_2 , suggesting the efficient production of O_2 . As shown in Fig. 3E, the fluorescence intensity of Ru(ddp) decreased in the presence of H_2O_2 in the PTC-M group, whereas the presence of H_2O_2 in the PTC-alone group showed little decrease in fluorescence (Fig. 3F), confirming the catalase activity resulting in oxygen production in PTC-M. Finally, we confirmed the H_2O_2 elimination property of PTC-M using an oxygen detection meter. As shown in Fig. 3G, the oxygen production by PTC-M was increased within the initial time, followed by a slow increase whereas the empty micelles PTC did not show oxygen production. The disproportionation of H_2O_2 was observed by the formation of oxygen bubbles in the PTC-M group as shown in Additional file 1: Figure S11A. It was also observed that PTC-M showed a higher production of oxygen compared to dMn_3O_4 alone, probably because of the close packing of dMn_3O_4 in PTC-M, making it more available for the reaction compared to free dMn_3O_4 (Additional file 1: Figure S11B). Even though the nanomicelles had loosened up due to H_2O_2 treatment, as shown in FE-TEM, dMn_3O_4 may still have been present inside the PTC-M, resulting in high catalase activity compared to free dMn_3O_4 . All these results together confirmed the superior catalase-mimicking activity of the PTC-M.

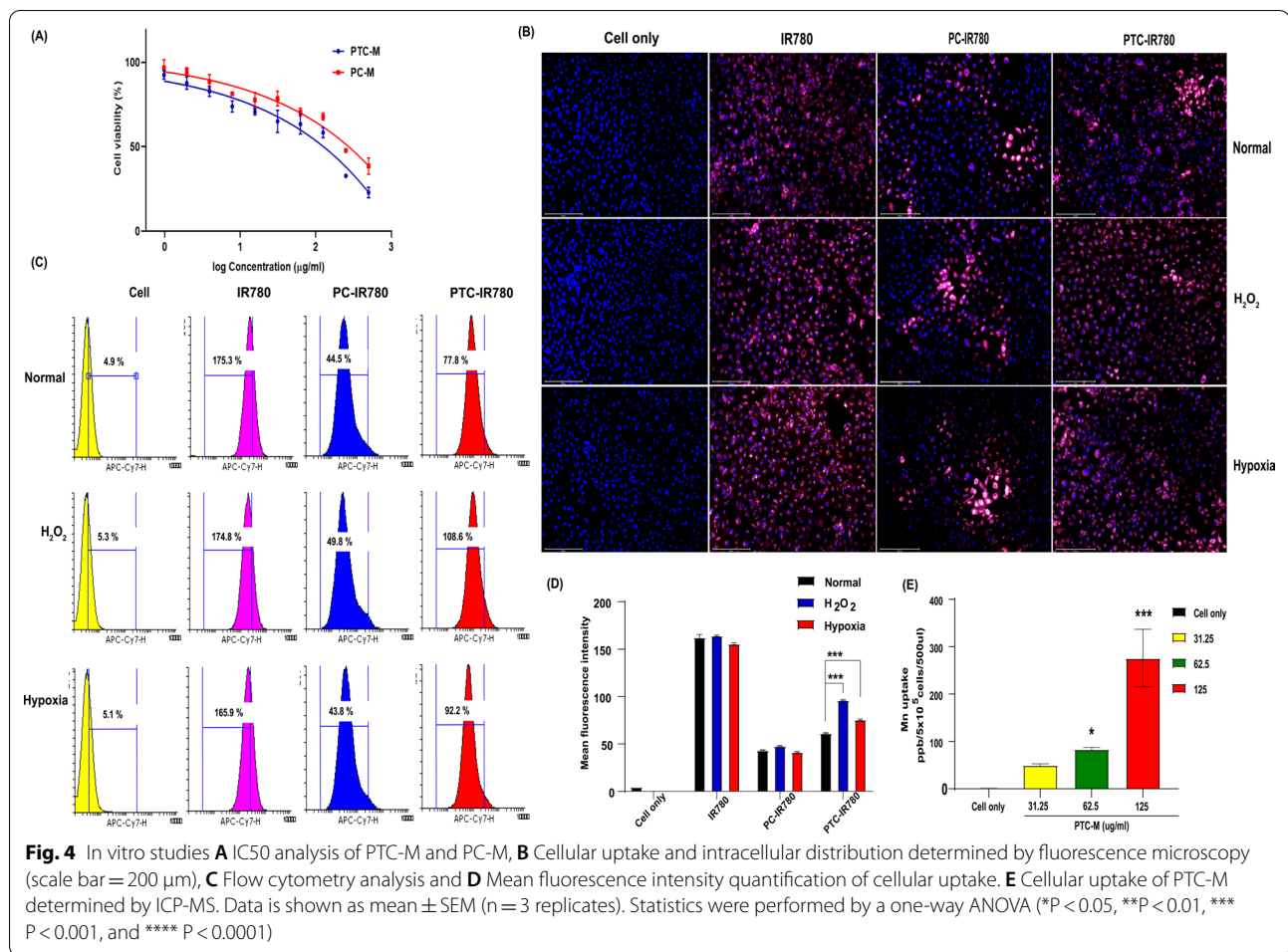
In vitro cell viability and cellular uptake

To confirm the cellular uptake and, ROS susceptibility of intracellularly distributed ROS-sensitive-PTC and the release pattern of the payload, we compared PTC with PC in *in vitro* conditions. First, we checked the cell viability of the prepared PTC, PC, PTC-M, and PC-M in HK-2 cells by the WST-1 assay (Additional file 1: Figure S12). The empty micelles underwent little cell death, but after dMn_3O_4 -loading, the cell viability decreased but the change was not statistically significant. Since the empty micelles were not cytotoxic, the slight variation in cell viability could be because of the surface-adsorbed dMn_3O_4 .

The IC₅₀ value of PTC-M and PC-M was determined to be 130.41 and 247.17 $\mu\text{g/ml}$, respectively (Fig. 4A). To further examine the intracellular uptake and distribution of the nanomicelles, IR780 was used as a model drug and prepared IR780 loaded PTC nanomicelles, PTC-IR780 to visualize the fluorescence intensity of IR780 using fluorescence microscopy (Evos FL Auto 2, Thermo Fisher Scientific, USA) (Fig. 4B). As a control group, we also analyzed the uptake of ROS-non-sensitive PC-IR780. Compared to PC-IR780, PTC-IR780 showed a higher uptake in HK-2 cells (Additional file 1: Figure S13). The exact reason behind the enhanced uptake of PTC-IR780 in non ROS condition is not clear, however it could be because the PTC could show slight sensitivity to the normal ROS level in cell culture conditions leading to PEG de-shielding leaving the surface charge slightly positive. PC-IR780 showed a similar uptake pattern regardless of ROS induced by H_2O_2 treatment or hypoxia-induced ROS conditions because of the non sensitive nature whereas, PTC-IR780 showed a different distribution pattern inside the cells, which could be due to the enhanced release of IR780 inside the cells. The previous cell viability data (Additional file 1: Figure S11) showing increased cell death in PTC-M would be also because of the enhanced cell uptake of PTC compared to PC. IR780 iodide, which is a highly hydrophobic dye that can show high affinity towards the cell membrane and showed a very bright signal regardless of the ROS exposure. The cellular uptake was further analyzed by checking the mean fluorescence intensity (MFI) by fluorescence-activated cell sorting (FACS) analysis (Fig. 4C), which supported the data obtained by fluorescence microscopy. As shown, the MFI was highest in the ROS-sensitive PTC-IR780 group compared to the other groups, confirming the enhanced release of IR780 in cells. We further quantified the MFI from various groups (Fig. 4D) which supported the microscopy data suggesting that PC-IR780 did not exhibit any significant difference in cellular uptake even under ROS induced conditions whereas, the PTC-IR780 showed a significant increase in cellular uptake when treated under ROS induced conditions. The cellular uptake of PTC was also determined by checking residual Mn in the cells after treatment with PTC-M. As shown in Fig. 4E, PTC-M showed a concentration-dependent uptake in the HK-2 cells. These results thus summarize the enhanced internalization of nanomicelles and accelerated release inside the cells probably due to the ROS mediated disassembly of nanomicelles.

Effect of PTC-M nanozyme on inflammation and apoptosis in hydrogen peroxide-stimulated HK-2 cells

We conducted *in vitro* studies in HK-2 cells to further explore the effects of PTC-M on oxidative stress



conditions at the cellular level. HK-2 cells were stimulated with H_2O_2 , a representative ROS (Fig. 5A). H_2O_2 enhanced heme oxygenase (HO)-1 expression, which was ameliorated by PTC-M co-treatment (Fig. 5A). The 2',7'-dichlorodihydrofluorescein diacetate (DCF-DA) assay was performed to check the pattern of intracellular ROS change. The HK-2 cells stimulated by H_2O_2 showed high fluorescence intensity, but after co-treatment with PTC-M, the fluorescence intensity was decreased (Fig. 5B). The BAX/BCL-2 ratio was increased by H_2O_2 treatment, which was also recovered

by PTC-M cotreatment, indicating protection against apoptosis (Fig. 5C). HK-2 cells treated with H_2O_2 exhibited a significant progressive increase in annexin V⁺/PI⁻ staining, which was prevented by PTC-M (Fig. 5D). H_2O_2 -induced ERK, JNK, and p38 phosphorylation was also suppressed by co-treatment with PTC-M, although a significant reduction in phosphorylated P38 was not observed (Fig. 5C). These data suggest that PTC-M suppressed ROS-induced apoptotic processes in renal tubular epithelial cells.

(See figure on next page.)

Fig. 5 Effects of PTC-M on inflammation, apoptosis and MAPK pathway in H_2O_2 treated HK-2 cell. **A** Comparison of expression level for HO-1 proteins determined by immunoblotting in HK-2 after stimulation with vehicles or H_2O_2 . β -actin was used as the endogenous control. **B** Images of the effects of H_2O_2 -induced ROS production by PTC-M imaged by fluorescence microscope. Cytosolic ROS was labeled using DCF-DA probes. **C** Comparison of expression level for apoptosis and MAPK proteins determined by immunoblotting in HK-2 after stimulation with vehicles or H_2O_2 . **D** Flow cytometry results with Annexin V-FITC/PI staining. Apoptotic cells were defined as Annexin V⁺ and PI⁻. Data are shown as mean ± SEM. *P < 0.05 vs. control (CON) group; #P < 0.05 vs. H_2O_2 group; †P < 0.05 vs. PTC-M group. HO-1 heme oxygenase-1, DCF-DA 2',7'-dichlorodihydrofluorescein diacetate, MAPK mitogen-activated protein kinase

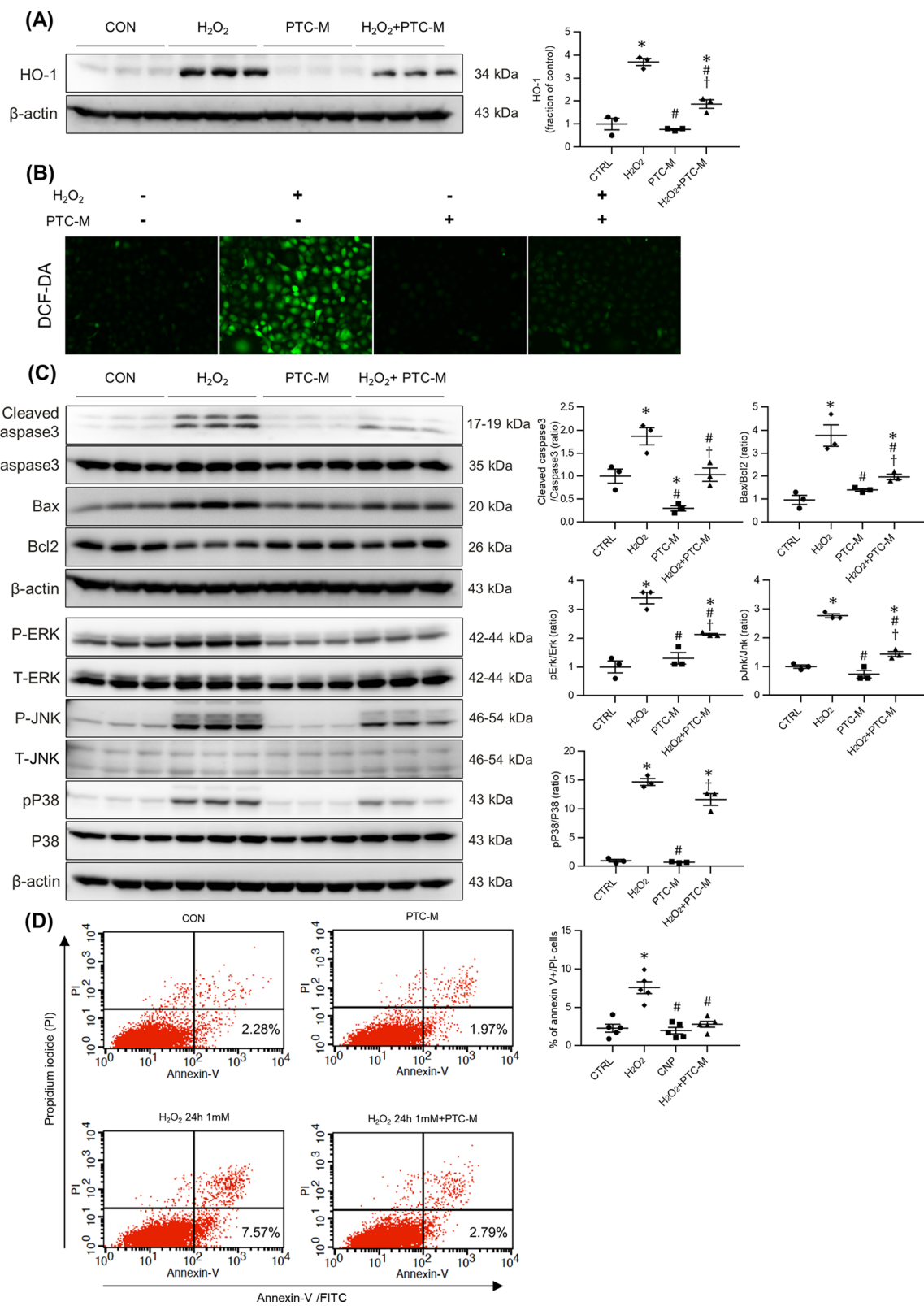


Fig. 5 (See legend on previous page.)

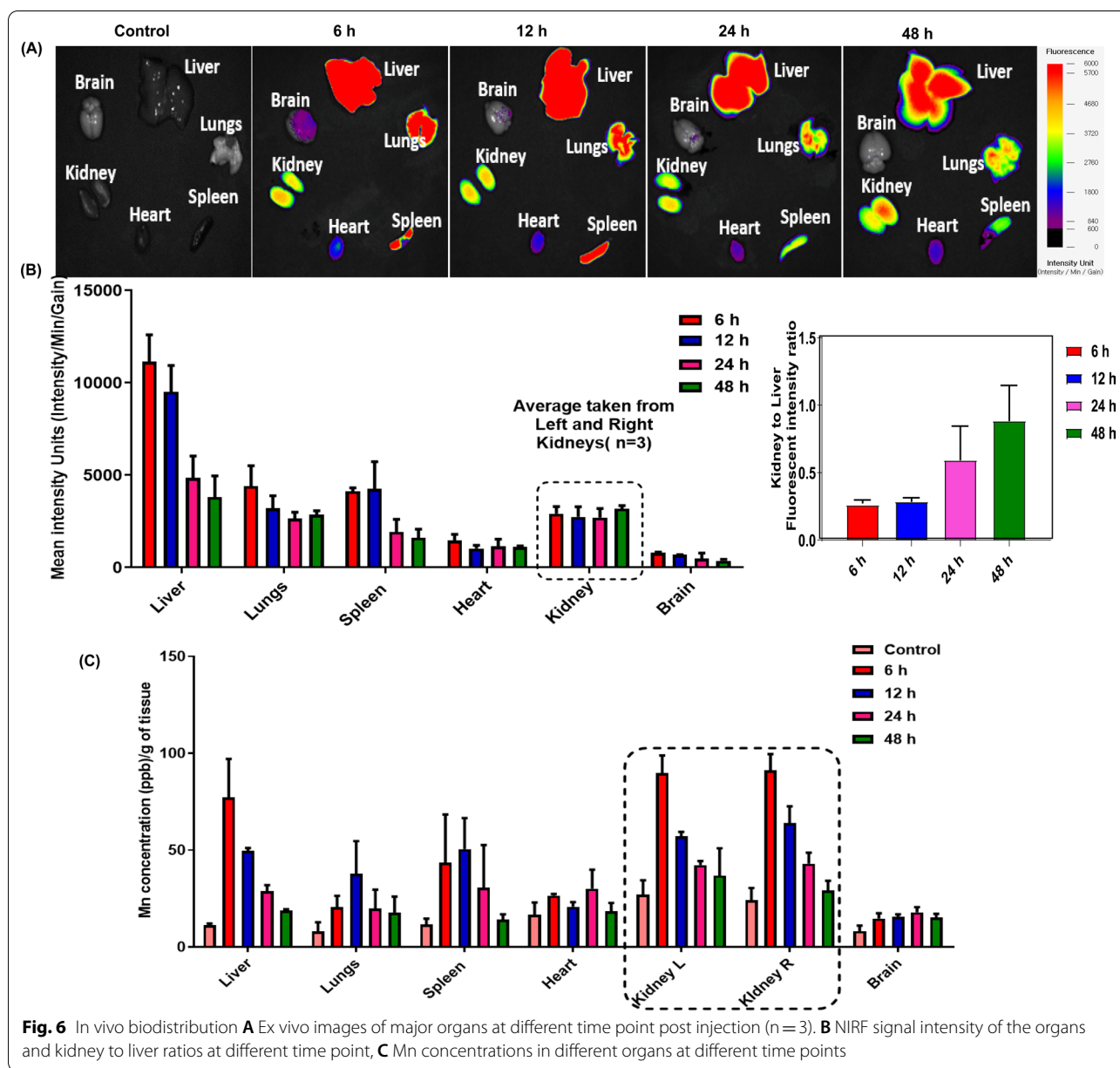


Fig. 6 In vivo biodistribution **A** Ex vivo images of major organs at different time point post injection (n = 3). **B** NIRF signal intensity of the organs and kidney to liver ratios at different time point, **C** Mn concentrations in different organs at different time points

Biodistribution of PTC-M nanozyme in IRI mice

The biodistribution of PTC was investigated in IRI mice by loading the fluorescent dye IR780 as a model drug (PTC-IR780). We also compared the biodistribution of the PC-IR780 and IR780 alone and observed that all groups showed fluorescence in major organs however PTC-IR780 showed an enhanced accumulation in kidney unlike PC-IR780 or IR780 group (Additional file 1: Figure S14 A). We also checked the biodistribution profile of PTC-IR780 in normal mice and found that it showed higher liver accumulation which is common for the nanoparticle after intravenous injection but

has not accumulated much in kidneys (Additional file 1: Figure S15). Thus, we conclude that the enhanced kidney accumulation of PTC is predominantly mediated by kidney inflammation. In our study, we designed PTC nanomicelles in such a way that it circulates in blood and gradually accumulates at the inflammation site and after reaching the inflammation site, the PTC gets destabilized by the presence of enhanced ROS and the loaded IR780 will be released which stays in the kidney for a longer time resulting in enhanced fluorescence. The kidney accumulation among all groups were compared by quantifying the ex-vivo fluorescence intensity and observed

that PTC showed a superior kidney accumulation even though it shows fluorescence in other major organs which is inevitable in case of systemic injection (Additional file 1: Figure S14 B) As shown in Fig. 6A, strong IR780 fluorescence intensity was observed in the kidneys from 6 h post-injection of PTC-IR780. The fluorescence intensity of the main organs was high in the order of liver, lungs, spleen, and kidneys. The fluorescence intensity of other organs decreased over time, while the fluorescence intensity of the kidneys remained relatively constant until 48 h. Thus, the fluorescence intensity of the kidneys versus the liver tended to increase gradually over time (Fig. 6B). This could be consistent with previous studies reporting that an increase in kidney inflammation could lead to enhanced permeability of the vessels and hence, increased accumulation of NMs in the kidneys [16]. The biodistribution was further confirmed by checking the Mn content in different organs using inductive-coupled plasma mass spectrometer (ICP-MS) analysis. As shown in Fig. 6C, the Mn concentration in both kidneys peaked at 6 h post-injection and gradually declined until 48 h. When comparing the tissue Mn concentration with that of the other main organs, the kidneys reached a higher tissue Mn concentration than the liver, lungs, and spleen at any time point. To confirm the clearance of the PTC-M, we have performed the ICP-MS analysis of all organs, feces, and urine at the end of the study and after a week and we observed that major portion of the Mn was shown in intestine and feces. It was observed that the Mn clearance primarily took a hepatobiliary route rather than renal clearance. We assume that after accumulating in kidney the Mn_3O_4 nanoparticle gets degraded to Mn ions which follows the usual hepatobiliary clearance of Mn (Additional file 1: Figure S16)[17].

PTC-M nanozyme decreases kidney damage marker and attenuates morphological changes in IRI mice kidneys

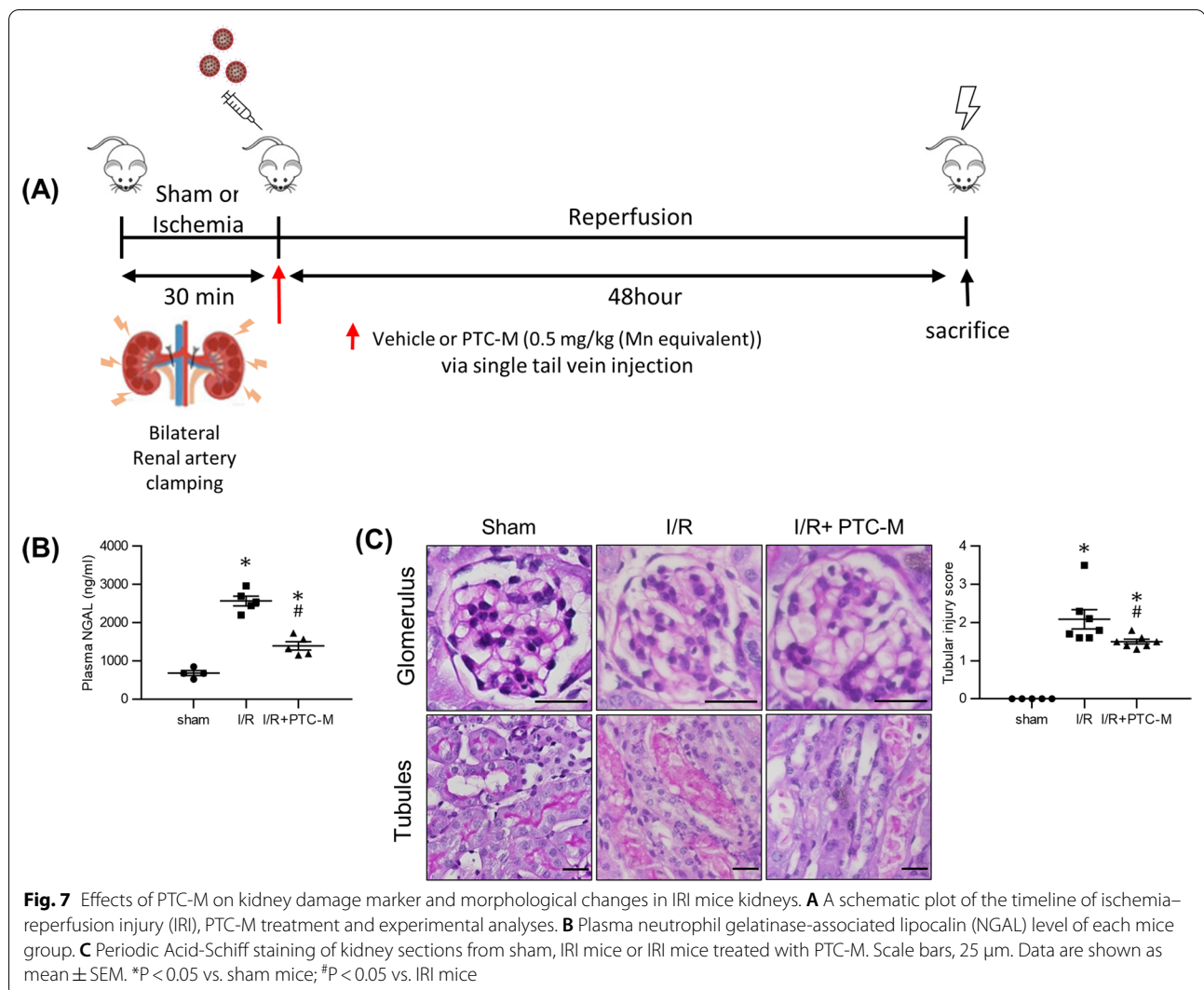
Finally, we performed an in vivo experiment to determine the efficacy of PTC-M to decrease renal damage in renal IRI. To investigate the overall status of damage in IRI kidneys, we measured plasma neutrophil gelatinase-associated lipocalin (NGAL), a well-known marker of tubular injury in AKI [18]. The level of plasma NGAL was significantly higher in the IRI group than in the sham group but was reduced by PTC-M treatment (Fig. 7B). We conducted periodic acid-Schiff (PAS) staining of the kidney sections to check for morphological changes (Fig. 7C). In contrast to the sham mice, renal tubular swelling, and dilatation filled with necrotic material were observed. Inflammatory cells infiltrating the interstitial spaces were observed in IRI mice kidneys. These changes were improved by PTC-M treatment. Tubular swelling, necrotic materials in the tubules, and inflammatory cell

infiltration were relatively attenuated in the PTC-M-treated IRI mice. Unlike changes in the tubules, there were no significant morphological differences observed in the glomeruli in each group.

PTC-M ameliorates inflammation and apoptosis in IRI mice kidneys

To examine whether the PTC-M could reduce the inflammation induced by the oxidative injury, we examined the protein expression level of HO-1 by western blot analysis to assess the degree of oxidative stress in IRI mice kidneys. We found considerably elevated expression levels of HO-1 in the kidneys of IRI mice, which were attenuated by PTC-M treatment (Fig. 8A). Immunohistochemical staining for HO-1 showed its increased expression in the mesangium of the glomeruli, periglomerular spaces, and peritubular interstitial space of IRI mice kidneys, which was reduced in PTC-M-treated mice kidneys (Fig. 8C). To elucidate the active inflammation in the kidneys of IRI mice, we checked the transcript levels of proinflammatory cytokines and adhesion molecules by quantitative polymerase chain reaction (qPCR) analysis (Fig. 8B). The mRNA expression levels of interleukin (IL)-6, monocyte chemoattractant protein (MCP)-1, tumor necrosis factor (TNF)- α , intracellular adhesion molecule (ICAM)-1, vascular cell adhesion molecule (VCAM-1), and transforming growth factor (TGF)- β were significantly increased in the kidneys of IRI mice, and the treatment with PTC-M suppressed these changes (Fig. 8B). Immunohistochemical staining for F4/80, a marker of murine macrophages, revealed increased expression in the periglomerular and interstitial spaces of the kidneys of IRI mice, which was also attenuated by PTC-M treatment (Fig. 8C). These data suggest that PTC-M suppressed renal inflammation and oxidative stress in IRI mice.

To evaluate the degree of renal tubular cell death in IRI mice, protein expression level of apoptotic proteins was assessed. Immunoblotting revealed an increased Bax/Bcl-2 ratio and cleaved caspase 3/caspase 3 ratio in the kidney tissue of IRI mice, suggesting that apoptosis was exacerbated (Fig. 9A). These changes were not observed in the mice treated with PTC-M. PTC-M treatment significantly reduced apoptotic cascades in kidney of IRI mice induced by oxidative stress. To determine whether PTC-M inhibited ROS-mediated apoptosis via mitogen-activated protein kinase (MAPK), we estimated changes in the MAPK signaling pathway. We performed immunoblot analysis for MAPK pathway protein level and their phosphorylated (activated) forms (Fig. 9B). The levels of phosphorylated ERK, JNK, and P38 were enhanced in the kidneys of IRI mice compared to the sham mice, which



were attenuated by PTC-M, although a significant reduction in phosphorylated JNK was not observed. Terminal deoxynucleotidyl transferase dUDP nick-end labeling (TUNEL) staining demonstrated more TUNEL-positive tubular epithelial cells in the cortex of the kidneys of IRI mice compared to that of sham mice, whereas PTC-M treatment decreased the numbers of TUNEL-positive cells (Fig. 9C). These results suggest that PTC-M reduced apoptosis in IRI mice kidneys by affecting the MAPK signaling pathway. These findings in IRI mouse kidneys were consistent with the results in H_2O_2 -stimulated human kidney cells, demonstrating a common mechanism of PTC-M renal protection. H&E staining was performed on major organs collected from normal and PTC-M treated group and no major histological changes indicating damages were observed (Additional file 1: Figure S17).

Discussion

The results of present study revealed that PTC-M could ameliorate the injury of kidney in IRI mice as representative experimental model of AKI. Especially, PTC-M significantly reduced inflammation and apoptosis in the kidneys of IRI mice and protected against H_2O_2 -induced cellular injury in human proximal tubular epithelial cells. These findings highlight the potential of PTC-M nanozyme as a candidate for therapeutic agent not only for IRI but also for AKI due to other causes.

Mn_3O_4 nanoparticles possess double-oxidation state Mn^{2+} and Mn^{3+} and protect the cells from ROS-mediated damage by preventing oxidative damage of the cellular components during high oxidative stress conditions. Apart from these benefits, the synthesis procedure of Mn_3O_4 is simple, where even a weak base can induce its formation [19–21]. Despite the great promise, Mn_3O_4 -based nanoparticles have not been exploited

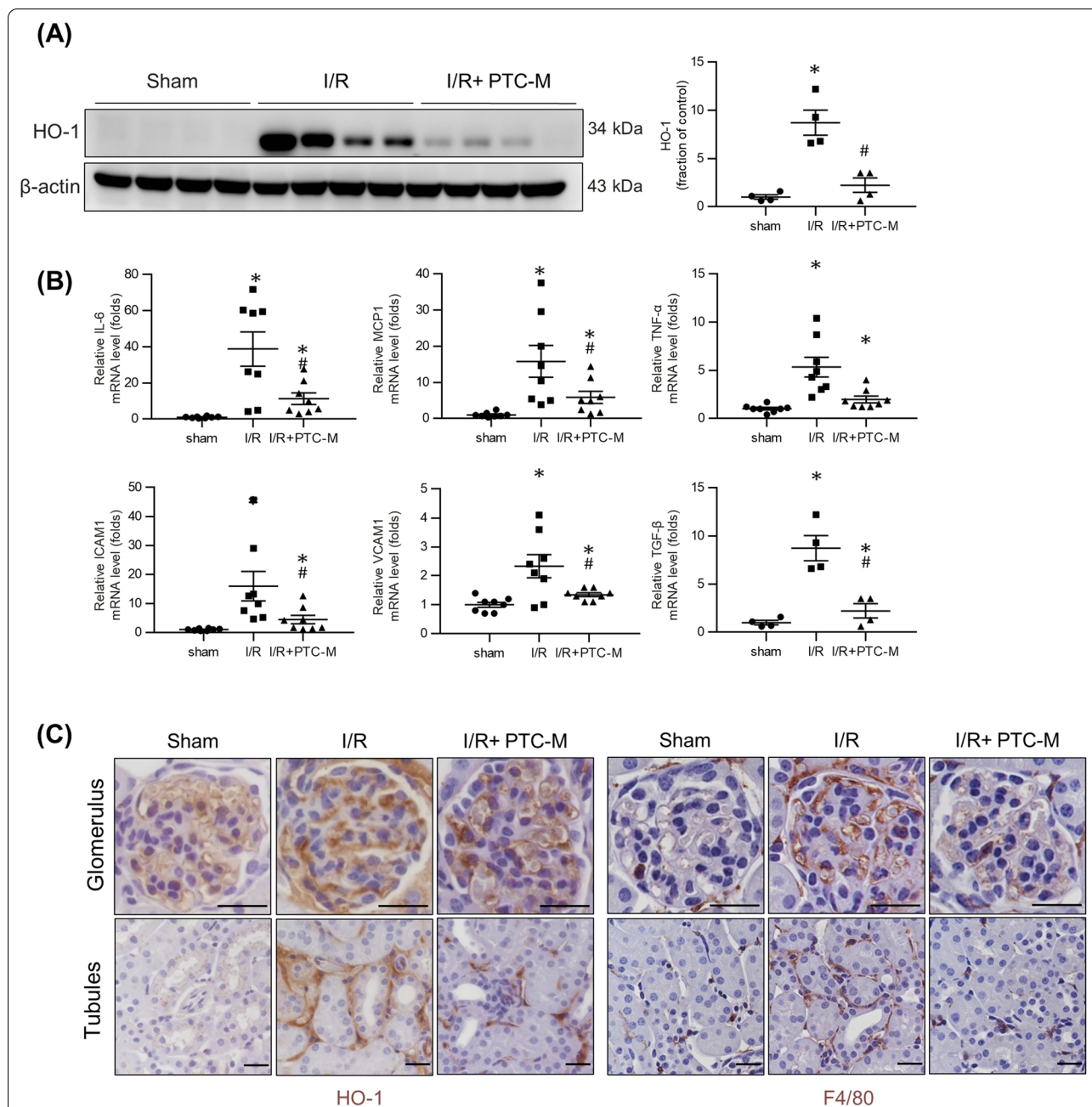
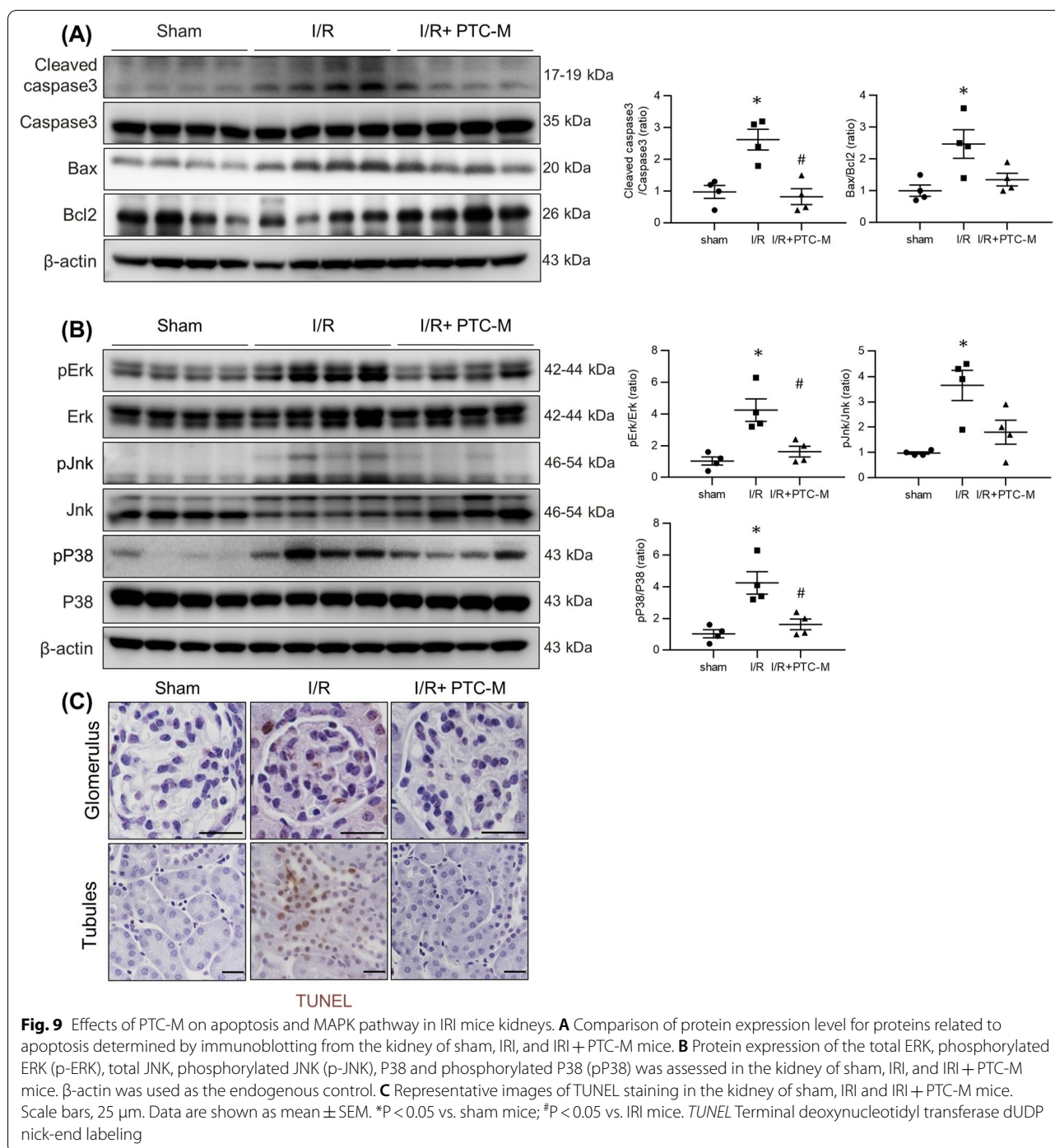


Fig. 8 Effects of PTC-M on inflammation in IRI mice kidneys. **A** Comparison of protein expression level for HO-1 determined by immunoblotting from the kidney of sham, IRI, and IRI + PTC-M mice. β -actin was used as the endogenous control. **B** Comparison of mRNA expression level for inflammatory markers determined by qPCR from the kidney of sham, IRI, and IRI + PTC-M mice. **C** Representative images of immunohistochemical staining for HO-1 (left) and F4/80 (right) in the kidney of sham, IRI and IRI + PTC-M mice. Scale bars, 25 μ m. Data are shown as mean \pm SEM. *P < 0.05 vs. sham mice; #P < 0.05 vs. IRI mice. *MCP-1* monocyte chemoattractant protein-1, *TNF- α* tumor necrosis factor- α , *ICAM-1* intercellular adhesion molecule-1, *VCAM-1* vascular cell adhesion molecule-1, *TGF- β* transforming growth factor beta

much for in vivo applications. Previously, the ROS-scavenging property of Mn_3O_4 nanoparticles was utilized for cytoprotection [22], for developing bio-semiconductors [20], and for relieving oxidative stress in plants [23]. However, the small particle size and the instability or possible

agglomeration of these nanoparticles can adversely affect the proper distribution and circulation half-life when used in in vivo conditions. Since ordinary Mn_3O_4 cannot be targeted, the potential toxicity to unwanted sites due to higher dosages could also be a safety concern in in vivo



conditions. Hydrophobically modified Mn_3O_4 NPs can ease this situation by allowing them to get loaded into a nanocarrier, thereby endowing it with the ability to passively target the site of action. Here, we synthesized 1-dodecanethiol stabilized hydrophobic Mn_3O_4 nanoparticles (d Mn_3O_4 NPs) and utilized their catalase-like activity to reduce kidney damage from IRI.

Recently, TK linkers have gained attention in developing ROS-responsive delivery systems to ROS-rich inflammation sites. TK bonds will be cleaved instantly by ROS oxidants, resulting in the loss of structural integrity of nanoparticulate systems, accelerating the release of loaded therapeutic agents [24–26]. Moreover, TK bonds are stable under physiological conditions. In this work,

we utilized an ROS-sensitive amphiphilic polymer PEG-stearamine conjugate developed by hydrophilic PEG connected to hydrophobic C18 alkyl chains via a TK linker (PEG-TK-C18, PTC) previously synthesized by our group [15]. ROS-sensitive nanomicelles were constructed by the self-assembly of PTC and the prepared dMn_3O_4 NPs were loaded inside, resulting in a versatile nanoplatform-ROS-sensitive nanozyme, PTC-M. The prepared PTC-M nanozyme contained different domains (as shown in Fig. 1): (1) the outer PEG shell endowed biocompatibility, dispersity, and prolonged circulation half-life in vivo and selective accumulation in inflammatory sites via extravasation through leaky vasculature and subsequent inflammatory cell-mediated sequestration (ELVIS) [27], (2) the TK linker, which is cleavable in an ROS-rich environment, (3) the C18 segment offering a hydrophobic core for incorporating dMn_3O_4 NPs as well as enhanced cell uptake, and (4) dMn_3O_4 NPs for ROS elimination. The other advantages included the simple synthesis procedure of dMn_3O_4 NPs. After administration, PTC-M circulated in the blood and accumulated at the ROS-rich inflammatory sites, followed by the instantaneous dissociation of TK linkage by ROS and destabilization of PTC-M, enabling the stepwise release and activation of the dMn_3O_4 NPs.

The characteristics of renal IRI are active inflammation by immune responses to ischemic tissue injury and elevated oxidative stress. Reduced tissue perfusion leads to acute tubular injury, which triggers inflammatory consequences and induces tubular epithelial cell death. These damaged cells amplify the inflammatory response again and create a vicious cycle. It is well known that the balance between pro-inflammatory and anti-inflammatory mediators determines tissue injury or repair [28]. Our study showed the upregulation of HO-1 in IRI mice kidneys, which was suppressed by PTC-M. HO-1, known as an endogenous anti-inflammatory enzyme, modulates immune responses following ischemia [29, 30]. The increased expression of HO-1 represents anti-inflammatory and antioxidative responses against IRI. The reduction in HO-1 expression by the administration of PTC-M indirectly implied a decrease in the inflammatory response in the tissues. In contrast, IL-6, MCP-1, and TNF- α are known as pro-inflammatory mediators and play roles in exacerbating tissue inflammation. ICAM-1 and VCAM-1 contribute to worsening inflammation by promoting the recruitment of inflammatory cells. PTC-M also reduced the expression of these molecules. Since these inflammatory cytokines trigger the systemic inflammation cascade, it is very important to suppress the inflammatory response to damaged kidneys.

The reestablishment of renal perfusion activates vascular endothelial cells, which triggers not only the release of

inflammatory cytokines but also the production of ROS [31]. Activated neutrophils also produce and release ROS through the activation of NADPH oxidase 2 by proinflammatory cytokines [32]. Excessive ROS causes damage to cellular proteins, lipids, nucleic acid, membranes, and mitochondria. The accumulation of intracellular ROS leads to oxidative stress conditions and the activation of cell death pathways. Thus, a reduction in tubular cell apoptosis is required for the treatment of renal IRI. The results of our study showed that the expression of the pro-apoptotic protein Bax was increased, and the expression of the anti-apoptotic protein Bcl-2 was decreased, resulting in an increase in the Bax/Bcl-2 ratio, consistent with previous studies [33]. PTC-M effectively attenuated IR-induced apoptosis, represented by a decrease in the Bax/Bcl-2 ratio. Cleaved caspase 3, an executioner caspase activated in both the extrinsic and intrinsic pathways, was also reduced by PTC-M treatment. The MAPK pathway is known to be involved in diverse cellular responses for survival against external stimuli. These responses include cellular proliferation, differentiation, inflammation, and apoptosis [34]. In previous studies, MAPK signaling pathways were activated after IR injury [35, 36]. In our results, the phosphorylation of ERK, JNK, and p38 MAPK was increased after IR injury and ameliorated by PTC-M treatment in both in vivo and in vitro experiments.

Conclusion

In summary, ROS-sensitive nanozyme PTC-M composed of hydrophobic dMn_3O_4 were successfully prepared and evaluated. PTC-M could passively target the kidneys and release dMn_3O_4 by responding to high levels of ROS present at the site, and the released dMn_3O_4 could scavenge the excessive ROS more effectively. Thus, PTC-M can overcome the shortcomings of dMn_3O_4 by increasing its solubility, stability, and biocompatibility, and can reduce the dose of dMn_3O_4 . It can also synergistically exert anti-inflammatory and anti-apoptotic effects. The present results demonstrated that PTC-M could ameliorate renal injury in IRI mice as an experimental model of AKI. Specifically, PTC-M effectively attenuated inflammation and apoptosis in the kidneys of IRI mice and protected against H_2O_2 -induced cellular injury in human proximal tubular epithelial cells. These findings highlight the potential of PTC-M as a therapeutic agent not only for IRI but also for AKI.

Materials and methods

Materials

Sodium hydroxide (NaOH), 1-Dodecanethiol, stearamine (C18), 1-ethyl-3-(3-dimethylaminopropyl) carbodiimide (EDC), N-hydroxysuccinimide (NHS), and

3-mercaptopropionic acid and triethylamine (TEA) were procured from Sigma-Aldrich (St. Louis, MO, USA). PEG-AM (2 KDa) was purchased from PEG-Shop (SunBio Inc., South Korea). Manganese (II) chloride dihydrate ($\text{MnCl}_2 \cdot 2\text{H}_2\text{O}$) and N, N-dimethylformamide (DMF) were purchased from Merck (Darmstadt, Germany). Tris (4,7-diphenyl-1,10-phenanthroline) ruthenium(II) dichloride ($\text{Ru}(\text{ddp})$) was purchased from ChemCruz (Santa Cruz Biotechnology, Texas, USA). Other solvents and reagents were of analytical grade and used as received.

Synthesis and characterization of dMn_3O_4 nanoparticles

dMn_3O_4 nanoparticles were prepared as follows. Briefly, 4 mmol NaOH in 2.5 ml of distilled water (DW) was added dropwise to 2 mmol MnCl_2 dissolved in 2.5 ml of DW under strong stirring with the solution turning brown. Later, 1 mmol of 1-dodecanethiol was added to the mixture during constant stirring till the solution became a paste. The precipitate was washed in ethanol by centrifugation at 5000 rpm for 5 min. Washing was repeated five times and the final pellet was dried, washed in DW twice, and lyophilized.

The morphology of the prepared dMn_3O_4 NPs was analyzed by FE-TEM, (JEM-2100F; JEOL, Tokyo, Japan) operated at 200 kV. To investigate the state of Mn in dMn_3O_4 , XPS analysis was performed using a k-alpha X-ray photoelectron spectrophotometer system (Thermo Fisher Scientific, Waltham, MA, USA). XRD measurements were performed using X-ray diffraction, M18XHF-SRA (MacScience, Japan), and the XRD pattern was analyzed using the ICDD (International Centre for Diffraction Data) file.

Synthesis and characterization of PTC and PC

The synthesis of TK linker, TK linker-conjugated polyethylene glycol (PEG-TK), and (PEG)-stearamine (C18) conjugate (PTC) was performed according to our previous publication [15]. As a control, we also prepared ROS-non-sensitive polymer (PC) by conjugating stearic acid to PEG-AM. Briefly, 200 mg of m-PEG amine was reacted with 160 mg of stearic acid with 160 μl of TEA, 480 mg of EDC, and 290 mg of NHS in 20 ml of DMF at 37 °C overnight with stirring under N_2 purging. The sample was then purified by dialysis (MWCO = 12–14 KDa) against DW for one day, followed by freeze-drying. The chemical structures of the synthesized PTC and PC were confirmed using proton nuclear magnetic resonance (^1H NMR) spectroscopy (400 Hz, Bruker: Billerica, MA, USA) in chloroform (CHCl_3). ROS-sensitive PTC and ROS-non-sensitive PC empty micelles were prepared by the self-assembly of PTC and PC under sonication and dialysis.

Preparation and characterization of ROS sensitive nanozyme (PTC-M)

PTC-M was prepared by the dialysis method. Briefly, 2 mg of dMn_3O_4 and 10 mg of PTC were dissolved in 1 mL of anhydrous dimethyl sulfoxide (DMSO). The mixture was then added dropwise to 20 ml of DW under probe sonication (30% amplitude, 5 s ON/OFF, 5 min). The solution was then dialyzed (MWCO = 12–14 KDa) against DW for one day, followed by freeze-drying. Similarly, dMn_3O_4 NP-loaded ROS-non-sensitive nanomicelles (PC-M) were also prepared as a control group. The hydrodynamic diameters and zeta potential of the prepared empty nanomicelles (PTC and PC) and dMn_3O_4 NP-loaded nanomicelles (PTC-M and PC-M) were evaluated by dynamic light scattering (Zetasizer Nano Z instrument, Malvern, UK). The morphology of the prepared PTC and PTC-M were visualized using FE-TEM. The ROS-sensitive destabilization via the degradation of the TK linker of PTC-M was observed by DLS and FE-TEM analysis after treating the samples with 1 mM H_2O_2 . The loading content of dMn_3O_4 in the final PTC-M was analyzed using a thermogravimetric analyzer (TGA N-1000, Scinco, Seoul, Korea) and an ICP-MS (820 ICP-MS Varian Bruker, Billerica, MA, USA) analysis.

The catalase-like activity of the final PTC-M was evaluated by observing the catalytic elimination of H_2O_2 by a fluorescent method using TA. Briefly, 1 mM H_2O_2 was added to the samples, followed by the addition of 0.5 mM TA (DMF). The samples were vortexed, and the fluorescence was recorded (excitation: 320 nm; emission: 425 nm) for up to 45 min. The catalase-like activity of PTC-M at different concentrations was also checked by a similar method.

H_2O_2 decomposition to water and oxygen was also confirmed using $\text{Ru}(\text{ddp})$ as a probe for oxygen generation. Briefly, 1 mM H_2O_2 was added to the samples, followed by the addition of 1 μM $\text{Ru}(\text{ddp})$ (DMF). The samples were mixed thoroughly and the fluorescence intensity at excitation 440 nm and emission 530 – 730 nm was recorded. Later, oxygen production was also confirmed by determining the dissolved oxygen concentration using a dissolved oxygen sensor (RDO Optical Dissolved Sensor, Thermo Scientific).

Cell culture and reagents

The *in vitro* studies were conducted as previously described [37]. In short, human renal proximal tubular epithelial cells (HK-2 cells, American Type Culture Collection, Manassas, VA, USA) were used for the *in vitro* studies. HK-2 cells were cultured and passaged every 3 – 4 days in 100-mm dishes containing a combination of Dulbecco's modified Eagle's (DMEM) and Hams F-12

medium (Welgene, Daegu, Korea) supplemented with 10% fetal bovine serum (FBS; Welgene), 100 U/ml penicillin, and 100 mg/ml streptomycin (Sigma-Aldrich). The HK-2 cells were then incubated in a humidified atmosphere of 5% CO₂ and 95% air at 37 °C for 24 h, and subcultured until 70 – 80% confluent. The HK-2 cells were plated onto 60-mm dishes in medium containing 10% FBS and incubated for 24 h. The cells were then incubated in DMEM-F12 medium without FBS and treated with H₂O₂ (1 mM) for an additional 24 h (except, 15 min for ERK, JNK, and p38). PTC-M (2 ug) was added 1 h prior to H₂O₂ treatment. All the in vitro experiments were repeated twice to determine reproducibility and done within the 30th passage of the cells.

Cell viability

In vitro cell viability was evaluated in HK-2 cells (1×10^4 cells/well) in DMEM F12 medium incubated overnight. The media was aspirated, and cells were incubated with different concentrations of PTC and PTC-M for 24 h followed by the WST-1 assay, performed according to the manufacturer's protocol. To compare the influence of TK linkages, we also compared the viability of cells treated with PC and PC-M. The IC₅₀ values of the samples were analyzed from the cell viability data. Non-treated cells were used as the positive controls and cells treated with 0.1% Triton \times 100 were used as the negative controls.

Cellular uptake

To investigate the intracellular distribution and release of payload from PTC, PTC loaded with a near-infrared (NIR) dye, IR780 iodide (PTC-IR780), was developed. For the uptake studies, HK-2 cells (3×10^4 cells/well) were seeded in Lab-Tek[®] Chamber Slides and incubated overnight. The media was aspirated, and different samples of IR780 only, PTC-IR780 and PC-IR780 with 4 ug/ml equivalent IR780 per well were added to the wells, followed by a 4-h incubation. Cells with no treatment were used as controls. After incubation, the media were aspirated, followed by DPBS washing and 4% paraformaldehyde (PFA) fixation. The cells were then counterstained with 4',6-diamidino-2-phenylindole (DAPI). The fluorescence intensity of IR780 was analyzed by fluorescence microscopy (Evos FL Auto 2, Thermo Fisher Scientific) to determine IR780 uptake by the cells. To show the ROS mediated destabilization of the nanomicelles and release of the fluorescent dye as a model drug, an oxidative stress injured HK2 cell model was used. The oxidative stress was induced by H₂O₂ treatment, 200 μ M H₂O₂ for 2 h or by exposing the cells under hypoxic environment by incubating the cells in a hypoxia chamber (1% O₂, 5% CO₂) for 24 h prior to treatment. Cellular uptake was further quantified by flow cytometry analysis. Briefly,

1×10^5 HK-2 cells/well were seeded in 12-well plates and incubated overnight. The media was aspirated, and different samples were added followed by 4 h incubation. The cells were then collected and centrifuged to obtain the pellet followed by two DPBS washes. The cells were then resuspended in FACS buffer containing 3% FBS and fluorescence-activated cell sorting (FACS) was performed to measure the uptake capability of each group. The data was gated with an APC-Cy 7 filter. Cellular uptake of the final PTC-M nanozyme was determined via ICP-MS analysis. Briefly, 1×10^5 of HK-2 cells/well were seeded in 12-well plates followed by overnight incubation. The media was then removed, and different concentrations of PTC-M were added to the wells and incubated for another 4 h. After the incubation, the cells were collected and centrifuged to obtain the pellet, which was washed with DPBS twice. Aqua regia (1 ml) was added to the final pellet for digestion and the samples were then diluted and analyzed for Mn content by ICP-MS. Non-treated cells were used as the controls.

Flow cytometry

Flow cytometry analysis was conducted as previously described [38]. An annexin V FLUOS staining kit (Sigma-Aldrich) was used to measure the level of annexin V binding according to the manufacturer's instructions. Briefly, after treatment with 0 or 1 mM H₂O₂ for 24 h with or without 2 ug of PTC-M pretreatment, HK-2 cells were harvested and washed twice with pre-cooled phosphate-buffered saline and resuspended in a binding buffer containing annexin V. After incubation in the dark for 15 min, the cells were analyzed by flow cytometry (Becton–Dickinson, San Jose, CA, USA). Several controls were used to optimize the instrument settings and determine the gating for the Windows-based platform. Apoptotic cells were defined as PI-negative and Annexin V-FITC positive.

Determination of intracellular ROS generation

To determine ROS generation, we used the fluoroprobe DCF-DA (Molecular Probes, Eugene, OR, USA) as previously described [38]. HK-2 cells were incubated with 0 or 1 mM H₂O₂ for 24 h with or without 2 ug of PTC-M pretreatment, and washed twice with Hank's balanced salt solution, then incubated with Hank's balanced salt solution (without phenol red) containing DCF-DA for 30 min at 37 °C in the dark. Images were obtained with a fluorescence microscope (Nikon, Tokyo, Japan).

Experimental animals and protocols

All experimental methods were performed in accordance with the relevant guidelines and regulations. The experimental protocol was approved by the Animal Care

Regulations Committee of Chonnam National University Hospital (CNUHIACUC-20009).

Seven-week-old male C57BL6 mice weighing 20–22 g were purchased from Samtako (Korea). The mice were housed at the animal care facility at Chonnam National University medical school and fed a standard diet with ad libitum access to water. The mice were divided into three groups: sham (n=4), IRI (n=4), and IRI with PTC-M treatment (n=4). To induce the IRI mice model, surgery was performed as follows. After anesthesia induction using an intraperitoneal injection of ketamine (70 mg/kg; Yuhan, Seoul, South Korea) and xylazine (7 mg/kg; Bayer, Leverkusen, Germany), a midline incision was made to expose the abdominal cavity and both renal pedicles were clamped with a micro clip (ROBOZ, Gaithersburg, MD, USA) for 30 min on a temperature-regulated table (38.5 °C) to maintain body temperature. The sham group (n=4) underwent the same procedure, except that the clip was not applied.

In vivo biodistribution

For biodistribution analysis, the IRI group was injected intravenously with PTC-IR780 at a dose of 0.5 mg/kg (IR780 equivalent). The mice were euthanized at predetermined times (6, 12, 24, and 48 h) and the major organs were collected. Fluorescence signals from the collected organs were analyzed using the fluorescence-labeled organism bio-imaging instrument (FOBI, NEO science, Gyeonggi, Korea). The fluorescence intensity of the anatomized key organs was measured to evaluate the organ accumulation of PTC-IR780. Biodistribution was further compared with PC-IR780 or IR780 after administering equivalent amount of IR780. The PTC-IR780 biodistribution was also compared in normal mice after intravenous administration.

Biodistribution analysis of the final PTC-M samples was also performed. Briefly, the IRI group was injected with 0.5 mg/kg of the PTC-M (Mn equivalent) samples, and the mice were euthanized at the predetermined time intervals mentioned above and the major organs were collected. The organs were then treated with aqua regia, and the samples were analyzed using ICP-MS to determine the tissue Mn concentration.

To check the therapeutic effect of PTC-M in vivo, the treatment group was given a single dose of 0.5 mg/kg PTC-M via tail vein injection after surgery. The mice were euthanized after 48 h of reperfusion. Blood samples were collected from the heart, and the left kidney was rapidly removed and processed for Western blotting or fixed in 4% paraformaldehyde solution for immunohistochemistry (IHC). The right kidney was frozen at –80 °C for real-time polymerase chain reaction (PCR) analysis.

Plasma NGAL measurement

Plasma neutrophil gelatinase-associated lipocalin (NGAL) levels were measured with a commercial ELISA kit (R&D Systems, Minneapolis, MN, USA) according to the protocol provided by the manufacturer. A 1:400 sample dilution was performed for the plasma NGAL measurements.

Semiquantitative immunoblotting

Western blot analysis was performed as previously described [37]. Kidney tissues were homogenized in ice-cold isolation solution containing 0.3 M sucrose, 25 mM imidazole, 1 mM ethylenediaminetetraacetic acid (EDTA), 8.5 mM leupeptin, and 1 mM phenylmethylsulfonyl fluoride (pH 7.2). The homogenates were centrifuged at 4000 × g for 15 min at 4 °C to remove whole cells, nuclei, and mitochondria. The total protein concentration was measured by a bicinchoninic acid (BCA) assay kit (Pierce; Rockford, IL, USA). All samples were adjusted to reach the same final protein concentrations. They were then dissolved at 65 °C for 15 min in sodium dodecyl sulfate (SDS)-containing sample buffer and stored at –20 °C. To confirm equal loading of the proteins, an initial gel was stained with Coomassie blue. SDS–polyacrylamide gel electrophoresis (PAGE) was performed on 9 or 12% polyacrylamide gels. The proteins were electrophoretically transferred onto nitrocellulose membranes (Hybond ECL RPN3032D; Amersham Pharmacia Biotech; Little Chalfont, UK) using a Bio-Rad Mini Protean II apparatus (Bio-Rad; Hercules, CA, USA). The blots were blocked with 5% milk in PBS-T (80 mM Na₂HPO₄, 20 mM NaH₂PO₄, 100 mM NaCl, and 0.1% Tween-20 at pH 7.5) for 1 h; incubated overnight at 4 °C with primary antibodies; and incubated with secondary anti-rabbit, anti-mouse, or anti-goat horseradish peroxidase-conjugated antibodies thereafter. The immunoblots were then visualized using an enhanced chemiluminescence system. Protein levels were quantified using densitometry. The relative intensities of the immunoblot signals were measured by densitometry using Scion Image for Windows software (Scion Corporation, 2000–2001, version Alpha 4.0.3.2, MD, USA) and expressed as fold-changes relative to the controls. The primary and secondary antibodies used in immunoblotting are listed in Table S1.

Real-time polymerase chain reaction (real-time PCR)

Polymerase chain reaction analysis was performed as previously described [37]. Renal cortexes were homogenized in Trizol reagent (Invitrogen, Carlsbad, CA, USA). RNA was extracted with chloroform, precipitated with isopropanol, washed with 75% ethanol, and then dissolved in DW. The RNA concentration was determined

by the absorbance at 260 nm (Ultraspec 2000; Pharmacia Biotech, Cambridge, UK). The mRNA expression of inflammatory cytokines and adhesion molecules was determined by real-time PCR. cDNA was made by reverse transcribing 5 µg of total RNA using oligo (dT) priming and superscript reverse transcriptase II (Invitrogen, Carlsbad, CA, USA). cDNA was quantified using a Smart Cycler II System (Cepheid, Sunnyvale, CA, USA) and SYBR Green was used for detection. Each PCR reaction was performed in 10 pM forward primer, 10 pM reverse primer, 2X SYBR Green Premix Ex Taq (TAKARA BIO INC, Seta 3-4-1, Japan), 0.5 µl cDNA, and H₂O to bring the final volume to 20 µl. The relative levels of mRNA were determined by real-time PCR, using a Rotor-Gene™ 3000 Detector System (Corbette research, Mortlake, NSW, Australia). The sequences of the primers are listed in Additional file 1: Table S2.

The PCR was performed according to the following steps: 1) 95 °C for 5 min; 2) 95 °C for 20 s; 3) 58 to 60 °C for 20 s (optimized for each primer pair), and 4) 72 °C for 30 s to detect SYBR Green. Steps 2 – 4 were repeated for an additional 40 cycles, while at the end of the last cycle, the temperature was increased from 60 to 95 °C to produce a melting curve. Data from the reaction were collected and analyzed with Corbett Research Software. The comparative critical threshold values from quadruplicate measurements were used to calculate the gene expression, with normalization to GAPDH as an internal control. Melting curve analysis was performed to enhance the specificity of the amplification reaction.

Histology

The preparation of kidney tissue proceeded as previously described [37]. Kidney tissues were fixed with 4% paraformaldehyde, embedded in paraffin, and cut into 3-µm-thick sections. Periodic acid-Schiff staining was performed according to the manufacturer's instructions (Abcam, Cambridge, MA, USA). For immunohistochemistry, deparaffinized tissue sections were antigen-retrieved by heating at 100 °C for 15 min in citrate buffer, pH 6.0 (Sigma-Aldrich). The sections were incubated overnight at 4 °C with primary antibodies diluted in blocking buffer (1% [w/v] bovine serum albumin dissolved in 0.3% [v/v] Triton X-100 prepared in PBS [0.3% PBS-T]). After the sections were briefly washed thrice with 0.3% PBS-T, they were incubated for 1 h at RT with secondary antibodies diluted in blocking buffer. Tubular injury scores were calculated by previously described method [39, 40]. Tubular injury score was measured by examination of ≥ 10 HPF of corticomedullary junction ($\times 200$ magnification) in PAS-stained sections (n = 5–7). The primary and secondary antibodies used in the immunohistochemical analyses are listed in Table S3.

Apoptosis of tubular epithelial cells was detected with TUNEL staining with ApopTag Plus Peroxidase In Situ Apoptosis Kit (Sigma-Aldrich), according to the manufacturer's instruction. Tissue sections of all major organs were collected paraffin embedded and were stained with hematoxylin/eosin (H&E) to compare the histological changes.

Statistical analysis

The results are expressed as the mean \pm standard error of the mean (SEM). Multiple comparisons among the three groups were performed using one-way analysis of variance (ANOVA) and the post-hoc Tukey's honestly significant difference test. Differences with p-values of less than 0.05 were considered significant.

Supplementary Information

The online version contains supplementary material available at <https://doi.org/10.1186/s12951-022-01410-z>.

Additional file 1: Figure S1. (A) Powder sample of prepared dMn₃O₄ (B) Schematic representation and (C) EDS analysis of dMn₃O₄. **Figure S2.** XPS analysis individual peaks in dMn₃O₄. **Figure S3.** NMR analysis (A) PTC and (B) PC. **Figure S4.** Low magnification FE-TEM images of (A) PTC (B) PC-M, PC-M + H₂O₂, PTC-M and PTC-M + H₂O₂. **Figure S5.** EDS elemental mapping of PTC-M. **Figure S6.** (A) Lyophilized sample of PTC-M (B) TGA analysis. **Figure S7.** (A) Hydrodynamic diameter and (B) zeta potential of PTC-M and PC-M before and after exposure to H₂O₂. **Figure S8.** (A) Hydrodynamic size distribution and (B) zeta potential of empty nanomicelles (PTC and PC) before and after treatment with H₂O₂. **Figure S9.** Stability of PTC-M in 10% FBS. **Figure S10.** Catalase like activity of PTC-M at different concentrations. **Figure S11.** (A) Disproportionation of H₂O₂ by PTC-M resulting in bubble formation (B) Dissolved oxygen production by dMn₃O₄ and PTC-M. Data is shown as mean \pm SEM (n = 3 replicates). Statistics were performed by a one-way ANOVA (*P < 0.05, **P < 0.01, *** P < 0.001, and **** P < 0.0001). **Figure S12.** In vitro cell viability of the empty nanomicelles (PTC, PC) as well as dMn₃O₄ loaded nanomicelles (PTC-M, PC-M). **Figure S13.** Cellular uptake and intracellular IR780 release. High magnification images (Scalebar=75µm). **Figure S14.** (A) Ex-vivo images of organs at different time points post injection from I/R model mice administered with PC-IR780 and IR780 (B) NIRF signal intensity quantification from isolated kidneys of PTC-IR780, PC-IR780 and IR780 administered mice in I/R model at different time points. **Figure S15.** Ex-vivo images of major organs at different time points post injection from normal C57 mice administered with PTC-IR780. **Figure S16.** ICP-MS analysis of major organs, feces and urine collected from AKI mice administered with PTC-M at 72 h and 168h. **Figure S17.** H & E staining of all major organs (liver, lung, spleen, heart, and intestine) collected from the control and PTC-M treated AKI mice (at 72 h), scale bar = 200 µm. **Table S1.** List of primary and secondary antibodies for immunoblotting. **Table S2.** List of primer sequences for real-time qPCR. **Table S3.** List of primary and secondary antibodies for immunohistochemistry.

Author contributions

IKP, EHB, SWK and HSC conceived and designed the experiments. HSC, APJ, SJ, AV, IJK and SAG performed the experiments, analyzed the data, and performed statistical analysis. HSC, APM wrote and edited the paper. SHS, CSK, SKM, SWK, IKP and EHB provided supervision and administration.

Funding

This research was supported by Basic Science Research Program through the National Research Foundation of Korea (NRF) grant funded by the Korea government, MSIT (NRF-2022R1C1C1007573 and NRF-2019R1F1A1041451)

and by a grant (CRI18038-1 and BCRI21056) of Chonnam National University Hospital Biomedical Research Institute. This work was partially supported by the National Research Foundation of Korea (NRF) grant funded by the Korea government (MSIT) (No. 2020R1A2C2005620, 2019R1A2C1003971 and 2020R1A5A2031185).

Availability of data and materials

All data generated or analyzed during this study are included in this published article and its Additional file 1. Research data are not shared.

Declarations

Ethics approval and consent to participate

All animal use procedures were carried out in accordance with the Animal Care Regulations Committee of Chonnam National University Hospital.

Consent for publication

All authors read and approve the final manuscript.

Competing interests

The authors declare that they have no competing interests.

Author details

¹Departments of Internal Medicine, Chonnam National University Medical School, 160, Baekseo-ro, Dong-gu, Gwangju 61469, Republic of Korea. ²Departments of Internal Medicine, Chonnam National University Hospital, Gwangju, Republic of Korea. ³Department of Biomedical Sciences, BK21 PLUS Center for Creative Biomedical Scientists, Chonnam National University Medical School, 160, Baekseo-ro, Dong-gu, Gwangju 61469, Republic of Korea. ⁴BioMedical Sciences Graduate Program (BMSGP), Chonnam National University, Hwasun-gun, Jeollanam-do, Republic of Korea.

Received: 1 November 2021 Accepted: 3 April 2022

Published online: 27 April 2022

References

- Kidney Disease: Improving Global Outcomes (KDIGO) Acute Kidney Injury Work Group. KDIGO Clinical Practice Guideline for Acute Kidney Injury. *Kidney Int Suppl.* 2012; 2:1–138.
- Togel F, Westenfelder C. Recent advances in the understanding of acute kidney injury. *F1000Prime Rep.* 2014;6:83.
- Susantitaphong P, Cruz DN, Cerda J, Abulfaraj M, Alqahtani F, Koulouridis I, Jaber BL, Acute Kidney Injury Advisory Group of the American Society of N. World incidence of AKI: a meta-analysis. *Clin J Am Soc Nephrol.* 2013;8:1482–93.
- Clermont G, Acker CG, Angus DC, Sirio CA, Pinsky MR, Johnson JP. Renal failure in the ICU: comparison of the impact of acute renal failure and end-stage renal disease on ICU outcomes. *Kidney Int.* 2002;62:986–96.
- Chawla LS, Eggers PW, Star RA, Kimmel PL. Acute kidney injury and chronic kidney disease as interconnected syndromes. *N Engl J Med.* 2014;371:58–66.
- Bonventre JV, Yang L. Cellular pathophysiology of ischemic acute kidney injury. *J Clin Invest.* 2011;121:4210–21.
- Castaneda MP, Swiatecka-Urban A, Mitsnefes MM, Feuerstein D, Kaskel FJ, Tellis V, Devarajan P. Activation of mitochondrial apoptotic pathways in human renal allografts after ischemiareperfusion injury. *Transplantation.* 2003;76:50–4.
- Perico N, Cattaneo D, Sayegh MH, Remuzzi G. Delayed graft function in kidney transplantation. *Lancet.* 2004;364:1814–27.
- Tanaka M, Sakata T, Palumbo J, Akimoto M. A 24-week, phase III, double-blind, parallel-group study of edaravone (MCI-186) for Treatment of amyotrophic lateral sclerosis (ALS). *Neurology* 2016; 86.
- Fu Z-Y, Wu Z-J, Zheng J-H, Li N, Lu J-Y, Chen M-H. Edaravone ameliorates renal warm ischemia-reperfusion injury by downregulating endoplasmic reticulum stress in a rat resuscitation model. *Drug Des Dev Ther.* 2020;14:175.
- Yao J, Cheng Y, Zhou M, Zhao S, Lin S, Wang X, Wu J, Li S, Wei H. ROS scavenging Mn₃O₄ nanozymes for in vivo anti-inflammation. *Chem Sci.* 2018;9:2927–33.
- Wei H, Wang E. Nanomaterials with enzyme-like characteristics (nanozymes): next-generation artificial enzymes. *Chem Soc Rev.* 2013;42:6060–93.
- Singh S. Nanomaterials exhibiting enzyme-like properties (nanozymes): current advances and future perspectives. *Front Chem.* 2019;7:46.
- Kim CS, Mathew AP, Uthaman S, Moon MJ, Bae EH, Kim SW, Park IK. Glycol chitosan-based renal docking biopolymeric nanomicelles for site-specific delivery of the immunosuppressant. *Carbohydr Polym.* 2020;241:116255.
- Uthaman S, Pillarsetti S, Mathew AP, Kim Y, Bae WK, Huh KM, Park I-K. Long circulating photoactivable nanomicelles with tumor localized activation and ROS triggered self-accelerating drug release for enhanced locoregional chemo-photodynamic therapy. *Biomaterials.* 2020;232:119702.
- Xu C, Chang A, Hack BK, Eadon MT, Alper SL, Cunningham PN. TNF-mediated damage to glomerular endothelium is an important determinant of acute kidney injury in sepsis. *Kidney Int.* 2014;85:72–81.
- Guroi KC, Aschner M, Smith DR, Mukhopadhyay S. Role of excretion in manganese homeostasis and neurotoxicity: a historical perspective. *Am J Physiol Gastrointest Liver Physiol.* 2022;322:G79–92.
- Haase M, Bellomo R, Devarajan P, Schlattmann P, Haase-Fielitz A, Group NM-al. Accuracy of neutrophil gelatinase-associated lipocalin (NGAL) in diagnosis and prognosis in acute kidney injury: a systematic review and meta-analysis. *Am J Kidney Dis.* 2009;54:1012–24.
- Lu W, Chen J, Kong L, Zhu F, Feng Z, Zhan J. Oxygen vacancies modulation Mn₃O₄ nanozyme with enhanced oxidase-mimicking performance for L-cysteine detection. *Sens Actuators B Chem.* 2021;333:129560.
- Chen X, Feng Q, Cai Q, Huang S, Yu Y, Zeng RJ, Chen M, Zhou S. Mn₃O₄ nanozyme coating accelerates nitrate reduction and decreases N₂O emission during photoelectrochemical denitrification by thiobacillus denitrificans-CdS. *Environ Sci Technol.* 2020;54:10820–30.
- Singh N, Savanur MA, Srivastava S, D'Silva P, Mughes G. A manganese oxide nanozyme prevents the oxidative damage of biomolecules without affecting the endogenous antioxidant system. *Nanoscale.* 2019;11:3855–63.
- Singh N, Savanur MA, Srivastava S, D'Silva P, Mughes G. A redox modulatory Mn₃O₄ nanozyme with multi-enzyme activity provides efficient cytoprotection to human cells in a Parkinson's disease model. *Angew Chem Int Ed.* 2017;56:14267–71.
- Lu L, Huang M, Huang Y, Corvini PF-X, Ji R, Zhao L. Mn₃O₄ nanozymes boost endogenous antioxidant metabolites in cucumber (*Cucumis sativus*) plant and enhance resistance to salinity stress. *Environ Sci Nano.* 2020;7:1692–703.
- Yang N, Xiao W, Song X, Wang W, Dong X. Recent advances in tumor microenvironment hydrogen peroxide-responsive materials for cancer photodynamic therapy. *Nano-Micro Lett.* 2020;12:15.
- Liang J, Liu B. ROS-responsive drug delivery systems. *Bioeng Transl Med.* 2016;1:239–51.
- Banstola A, Poudel K, Pathak S, Shrestha P, Kim JO, Jeong J-H, Yook S. Hypoxia-mediated ROS amplification triggers mitochondria-mediated apoptotic cell death via PD-L1/ROS-responsive, dual-targeted, drug-laden thioketal nanoparticles. *ACS Appl Mater Interfaces.* 2021;13(19):22955–69.
- He L, Qin X, Fan D, Feng C, Wang Q, Fang J. Dual-stimuli responsive polymeric micelles for the effective treatment of rheumatoid arthritis. *ACS Appl Mater Interfaces.* 2021;13(18):21076–86.
- Mulay SR, Kumar SV, Lech M, Desai J, Anders HJ. How kidney cell death induces renal necroinflammation. *Semin Nephrol.* 2016;36:162–73.
- Bolisetty S, Zarjou A, Agarwal A. Heme oxygenase 1 as a therapeutic target in acute kidney injury. *Am J Kidney Dis.* 2017;69:531–45.
- Nath M, Agarwal A. New insights into the role of heme oxygenase-1 in acute kidney injury. *Kidney Res Clin Pract.* 2020;39:387–401.
- Korthuis RJ. Mechanisms of I/R-induced endothelium-dependent vasodilator dysfunction. *Adv Pharmacol.* 2018;81:331–64.
- Schofield ZV, Woodruff TM, Halai R, Wu MC, Cooper MA. Neutrophils—a key component of ischemia-reperfusion injury. *Shock.* 2013;40:463–70.
- Borkan SC. The Role of BCL-2 family members in acute kidney injury. *Semin Nephrol.* 2016;36:237–50.

34. Pearson G, Robinson F, Beers Gibson T, Xu BE, Karandikar M, Berman K, Cobb MH. Mitogen-activated protein (MAP) kinase pathways: regulation and physiological functions. *Endocr Rev.* 2001;22:153–83.
35. di Mari JF, Davis R, Safirstein RL. MAPK activation determines renal epithelial cell survival during oxidative injury. *Am J Physiol.* 1999;277:F195–203.
36. Park KM, Chen A, Bonventre JV. Prevention of kidney ischemia/reperfusion-induced functional injury and JNK, p38, and MAPK kinase activation by remote ischemic pretreatment. *J Biol Chem.* 2001;276:11870–6.
37. Choi HS, Kim IJ, Kim CS, Ma SK, Scholey JW, Kim SW, Bae EH. Angiotensin-[1-7] attenuates kidney injury in experimental Alport syndrome. *Sci Rep.* 2020;10:4225.
38. Park JS, Choi HI, Bae EH, Ma SK, Kim SW. Paricalcitol attenuates indoxyl sulfate-induced apoptosis through the inhibition of MAPK, Akt, and NF- κ B activation in HK-2 cells. *Korean J Intern Med.* 2019;34:146–55.
39. Chen J, Chen JK, Conway EM, Harris RC. Survivin mediates renal proximal tubule recovery from AKI. *J Am Soc Nephrol.* 2013;24:2023–33.
40. Takaori K, Nakamura J, Yamamoto S, Nakata H, Sato Y, Takase M, Nameta M, Yamamoto T, Economides AN, Kohno K, et al. Severity and frequency of proximal tubule injury determines renal prognosis. *J Am Soc Nephrol.* 2016;27:2393–406.

Publisher's Note

Springer Nature remains neutral with regard to jurisdictional claims in published maps and institutional affiliations.

Ready to submit your research? Choose BMC and benefit from:

- fast, convenient online submission
- thorough peer review by experienced researchers in your field
- rapid publication on acceptance
- support for research data, including large and complex data types
- gold Open Access which fosters wider collaboration and increased citations
- maximum visibility for your research: over 100M website views per year

At BMC, research is always in progress.

Learn more biomedcentral.com/submissions

